JGR Solid Earth

RESEARCH ARTICLE
10.1029/2020JB019477

Depth-Dependent Azimuthal Anisotropy Beneath the Juan de Fuca Plate System

Zachary C. Eilon[1] and Donald W. Forsyth[2]

[1]Department of Earth Science, University of California Santa Barbara, Santa Barbara, CA, USA, [2]Department of Earth, Environmental, and Planetary Sciences, Brown University, Providence, RI, USA

Key Points:
- We use a two-plane wave method to measure azimuthal anisotropy as a function of depth across the Juan de Fuca and Gorda plate system
- Results are consistent with measured *SKS* splitting; our study offers depth sensitivity crucial to interpretation of underlying dynamics
- Regionalized patterns of anisotropy reveal substantial differences in ridge-derived fabric and how plates shear over underlying mantle

Supporting Information:
- Supporting Information S1

Correspondence to:
Z. C. Eilon,
eilon@ucsb.edu

Citation:
Eilon, Z. C., & Forsyth, D. W. (2020). Depth-dependent azimuthal anisotropy beneath the Juan de Fuca plate system. *Journal of Geophysical Research: Solid Earth*, *125*, e2020JB019477. https://doi.org/10.1029/2020JB019477

Received 27 JAN 2020
Accepted 12 JUN 2020
Accepted article online 15 JUN 2020

Abstract We use surface wave measurements to reveal anisotropy as a function of depth within the Juan de Fuca and Gorda plate system. Using a two-plane wave method, we measure phase velocity and azimuthal anisotropy of fundamental mode Rayleigh waves, solving for anisotropic shear velocity. These surface wave measurements are jointly inverted with constraints from *SKS* splitting studies using a Markov chain approach. We show that the two data sets are consistent and present inversions that offer new constraints on the vertical distribution of strain beneath the plates and the processes at spreading centers. Anisotropy of the Juan de Fuca plate interior is strongest (~2.4%) in the low-velocity zone between ~40- to 90-km depth, with ENE direction driven by relative shear between plate motion and mantle return flow from the Cascadia subduction zone. In disagreement with *Pn* measurements, weak (~1.1%) lithospheric anisotropy in Juan de Fuca is highly oblique to the expected ridge-perpendicular direction, perhaps connoting complex intralithospheric fabrics associated with melt or off-axis downwelling. In the Gorda microplate, strong shallow anisotropy (~1.9%) is consistent with *Pn* inversions and aligned with spreading and may be enhanced by edge-driven internal strain. Weak anisotropy with ambiguous orientation in the low-velocity zone can be explained by Gorda's youth and modest motion relative to the Pacific. Deeper (≥90 km) fabric appears controlled by regional flow fields modulated by the Farallon slab edge: anisotropy is strong (~1.8%) beneath Gorda, but absent beneath the Juan de Fuca, which is in the strain shadow of the slab.

Plain Language Summary Seismic waves travel across the surface of the planet with speeds that vary depending on the temperature and composition of the Earth's interior in the regions they traverse. In detail, we find that they sometimes also exhibit directional dependence of wave speed—they travel across the same location faster going in one direction than going in another. This directional dependence arises from the alignment (or "fabric") of crystals that make up the rocks tens and hundreds of kilometers beneath the surface. The fabric, in turn, relates to how rocks have moved over the last few millions of years, thereby allowing us to peer into the history of tectonic motions on our planet. We use a technique that provides rare information about how this fabric changes with depth and find substantial variations in fabric at different depths and locations within the Juan de Fuca plate boundary region. The variations are linked to the differences in strength of drag between the tectonic plates and the underlying mantle. We also find evidence that subducting slabs—cold plates that are in the process of sinking into the hotter interior of the planet—can interrupt and strongly modify the flow of the hot mantle around them.

1. Introduction

Seismic anisotropy holds great promise for teaching us about the structure, history, and ongoing dynamics of oceanic plates (e.g., Becker & Lebedev, 2019; Long & Becker, 2010; Nicolas & Christensen, 1987). Anisotropy is linked to inherent fabrics within oceanic crust and particularly mantle, where crystallographic preferred orientation (CPO) of individually anisotropic minerals confers directional dependence to seismic velocities, sometimes augmented by lithologic foliation (Mainprice & Nicolas, 1989). CPO, especially within olivine-rich aggregates, arises from time-integrated shear strain under dislocation creep conditions and therefore encodes the dynamic evolution of deforming oceanic mantle (e.g., Karato et al., 2008; Skemer & Hansen, 2016). Large-scale foliation within the mantle may be related to organized melt (e.g., Holtzman et al., 2003; Kendall et al., 2005), thus imparting details of melt content and local stress field.

The oceanic plates have a deceptively simple structure, formed by upwelling beneath mid-ocean ridges (MORs), corner flow, and slow conductive cooling as the plates spread away from the zones of divergence.

Simulations of this process that track finite strain and model fabric development suggest that lithospheric anisotropy with fast direction in the direction of spreading should develop within <100 km of the ridge axis (Blackman et al., 2002; Castelnau et al., 2009), a hypothesis supported by observations of spreading-parallel *SKS* splitting at fast spreading centers (Wolfe & Solomon, 1998) and highly extended continental rifts (Eilon et al., 2014).

In detail, however, the dynamics of this process are not clear. Adiabatic decompression melting that produces oceanic crust also dehydrates the upper mantle, theoretically leading to a substantial increase in viscosity shallower than the dewatering depth of ~60 km (e.g., Hirth & Kohlstedt, 1996) that could inhibit or modify shallow fabric development (Beghein, 2018). The presence and multiphase flow geometry of melt, feedbacks between rheology and grain size, and dynamic contributions to axial upwelling (with required off-axis downwelling) all further complicate deformation and may disrupt simple fabrics at the ridge axis (Auer et al., 2015; Blackman et al., 2002; Braun et al., 2000; Katz, 2010; Katz et al., 2006; Turner et al., 2015). Highly variable MOR shear wave splits measured from global data sets (Eakin et al., 2018; Nowacki et al., 2012) are consistent with more complex MOR anisotropic structure.

As oceanic plates mature, shear occurs between convecting mantle and the overlying oceanic lithosphere whose kinematics are mostly dictated by far-field slab pull (Forsyth & Uyeda, 1975). The depth of active deformation should be age-dependent; as plates cool, the zone of minimum viscosity and maximum strain should migrate to increasing depth (e.g., Becker et al., 2008; Schaeffer et al., 2016). Shallow asthenospheric fabrics generated by shear immediately beneath thin young plates might then be frozen into thickening lithosphere with possible post-strain fabric annealing (Boneh et al., 2017). On the other hand, some observations suggest that the oceanic plates' anisotropic character is determined close to the ridge and does not vary with age (Beghein, 2018; Beghein et al., 2014; Nettles & Dziewonski, 2008) perhaps owing to changes in dominant deformation mechanism (Hedjazian et al., 2017).

A substantial fraction of our knowledge of upper mantle anisotropy is derived from SK(K)S splitting observations, which in most situations comprise path averages with little depth sensitivity due to near-vertical ray paths. By contrast, surface waves offer constraints on depth dependency of anisotropic structure, albeit at the expense of substantial intrinsic horizontal smoothing.

Global (Montagner & Tanimoto, 1991; Debayle & Ricard, 2013; Auer et al., 2014; French & Romanowicz, 2014; Moulik & Ekström, 2014) or basin-wide (Beghein et al., 2014; Eddy et al., 2018; Nishimura & Forsyth, 1989) studies of surface wave anisotropy demonstrate broad agreement between observed fast directions and plate motions predicted by large-scale mantle flow models (Becker et al., 2014; Auer et al., 2015), but resolve only coarse (~1,000 km) structure due to long paths across the sparsely sampled oceans. Improvements in the reliability and volume of ocean bottom seismic data acquisition have more recently allowed high-resolution measurements of anisotropy at focused sites within the ocean basins (e.g., Gaherty et al., 1996; Lin et al., 2016; Takeo et al., 2016). These studies (e.g., Becker et al., 2014; Russell et al., 2019; Weeraratne et al., 2007) largely validate global models of strong fossil spreading-parallel lithospheric anisotropy overlying an asthenospheric layer wherein fabric aligns with plate motion relative to motion of underlying convecting mantle (often assumed to be equivalent to plate motion in a hotspot reference frame). Global compilations suggest that the depth of transition between these fabric regimes may be age dependent (and even a direct proxy for lithospheric thickness; e.g., Becker et al., 2014; Schaeffer et al., 2016), but this general trend has numerous exceptions and has not been fully validated close to spreading centers.

In this study, we use surface wave data from the dense Cascadia Initiative (CI) to measure anisotropy as a function of depth within subregions of the offshore Cascadia plate boundary. We jointly invert surface wave measurements with results from *SKS* splitting analyses, using a Bayesian approach and a simple layered structure that has only as many model parameters as our data are able to independently constrain. We interpret the robustly resolved structures in terms of local and regional dynamics.

2. Data and Previous Work

The CI (Toomey et al., 2014) instrumented the entire Juan de Fuca (JdF) and Gorda plates with broadband ocean bottom seismometers at a spacing of ~70 km from 2014–2018 (Figure 1). This diachronous 4-year

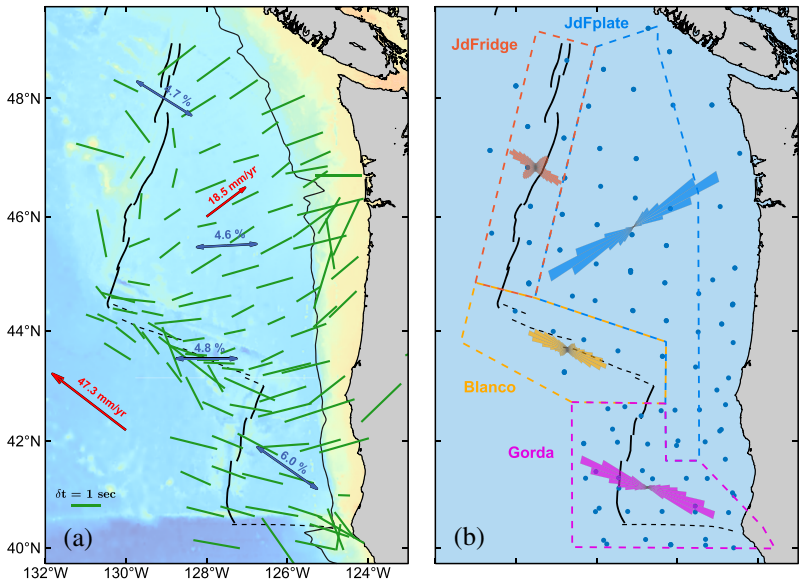

Figure 1. Overview of the field area. (a) Directional data important to the paper: green lines are shear wave splits from Bodmer et al. (2015); blue arrows are *Pn*-derived fast azimuths from VanderBeek et al. (2016) and VanderBeek and Toomey (2017, 2019); and red arrows show global strain rate model (GSRM) plate motion in a no-net-rotation frame (Kreemer et al., 2014). (b) Data for this study. Locations of Cascadia initiative OBS stations used in this study (blue dots), dashed areas show four primary regions in which average anisotropic structure was measured, named as indicated. Rose plots show radial histogram of surface wave fast directions for periods ≤50 s averaged over each subregion (see Figures 2, 3, S3, and S4); note the general similarity with *SKS* data.

seismic data set affords the most complete and dense coverage of an entire oceanic plate to date and is uniquely suited to the study of near-ridge oceanic anisotropy.

Detailed tomographic and structural studies of velocity, discontinuity, and attenuation structure of this region (e.g., Bell et al., 2015; Gao, 2016; Rychert et al., 2018; Janiszewski et al., 2019; and references below) allow us to place questions about anisotropic structure within a comprehensive seismological context: dynamic upwelling at the ridge axis is supported by high attenuation (Eilon & Abers, 2017; Ruan et al., 2018), the magnitude and morphology of low-velocity features (Byrnes et al., 2017), and a rapid off-axis increase in wave speed and decrease in attenuation attributed to downwelling-induced cooling and melt freezing (Bell et al., 2016; Byrnes et al., 2017; Ruan et al., 2018). The JdF and Gorda plates are subducting beneath North America at ~30–40 mm/yr to the NE, with ~15 mm/yr of rollback in an absolute reference frame (Kreemer et al., 2014; Wang et al., 2018). Low wave speeds beneath the forearc (Hawley et al., 2016) are interpreted as indicating subslab buoyant material flowing up the underside of the downgoing plate; in detail, concentration of this material at two zones inboard of Gorda and in the Northern Cascades may explain along-strike variations in subduction zone coupling (Bodmer et al., 2018).

Two studies have reported shear wave splitting observations of anisotropy in the JdF region using *SKS* data from the CI (Bodmer et al., 2015; Martin-Short et al., 2015), with generally similar results. There are distinct regional differences in the fast direction (Figure 1a): roughly ENE in the interior of the JdF plate, ESE in the Gorda part of the plate system and adjacent Pacific plate, and variable but more N-S near the JdF ridge axis. Bodmer et al. (2015) defined several oceanic subregions in which *SKS* splitting is approximately uniform (Figure 1b). *SKS* splitting is normally thought to arise primarily from anisotropic fabrics in the upper mantle where it deforms by dislocation creep; in this setting beneath young seafloor, we expect CPO to develop primarily in the upper 200 km where shear velocities are lowest (Figure 2a) and minimal viscosity results in maximal shear deformation.

Regional variations in anisotropy of the uppermost (<15-km depth) mantle are also shown by changes in the azimuthal pattern of *Pn* velocity across the study area (Figure 1a) (VanderBeek et al., 2016; VanderBeek &

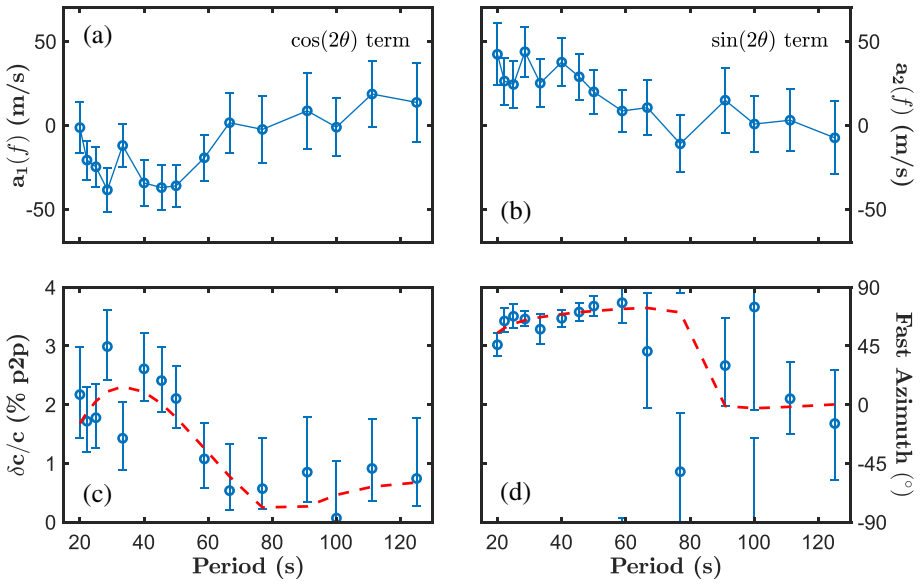

Figure 2. Dispersion curves of surface wave anisotropy within the JdFplate region. Top row shows raw measurements as (a) cosine, a_1 and (b) sine, a_2 coefficients of 2θ azimuthal variation in m/s. Bottom row shows the same data converted to (c) fractional peak-to-peak anisotropy amplitude and (d) fast azimuth. Whiskers show 2 standard deviation uncertainties. Red dashed lines show predicted values from full anisotropy model (Figure 4).

Toomey, 2017, 2019). However, the rotation in direction between the JdF and Gorda regions is similar in magnitude and sense to the rotation for *SKS* (Figure 1a). Within the interior of the JdF plate, *Pn* phases record >4.5% anisotropy beneath the Moho, with φ almost precisely E-W (VanderBeek & Toomey, 2017), while *SKS* data have mean δt of 1.0 s and φ = ~68° (Bodmer et al., 2015; Martin-Short et al., 2015), suggesting depth dependence of the anisotropic structure. These observed values are straddled by kinematically relevant azimuths that might have been expected to dominate internal fabric: absolute plate motion (APM) is further counterclockwise, at ~55 ± 5° according to no-net-rotation (Kreemer et al., 2014) or absolute (Wang et al., 2018) reference frames, while ridge-perpendicular (fossil spreading parallel)

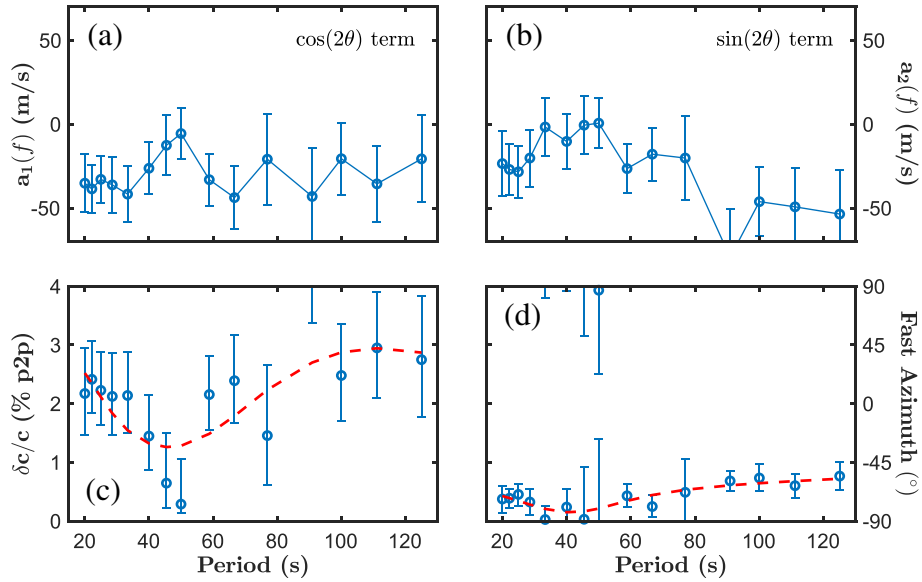

Figure 3. As for Figure 2, but for the Gorda region.

fabric should trend ~110°. In the Gorda region, *Pn* anisotropy tomography shows a clockwise rotation of fast axes from spreading parallel (~90°) at the Gorda ridge to ~130° within the plate, commensurate with internal shear of the Gorda lithosphere (VanderBeek & Toomey, 2019), which has strongly internally deformed since 2–3 Ma (Wilson, 1989).

To obtain more information about the depth dependence of anisotropy, we employ the frequency dependence of azimuthal anisotropy of Rayleigh waves at 16 periods in the range 20 to 125 s, in combination with the *SKS* data of Bodmer et al. (2015). We use Rayleigh wave data from Bell et al. (2016), who used a two-plane wave method to measure wavefield properties at periods from 20 to 143 s across the study region from 78 carefully selected earthquakes measured during the first 3 years of the CI deployment. This data set was augmented by data from the fourth year of the CI deployment as in Ruan et al. (2018), which greatly improves resolution in the southern half of the study area including Gorda, the Blanco fracture zone region, and the southern part of the JdF plate. The data set has good back azimuthal distribution of events (see Figure 1 of Ruan et al., 2018). In brief, we select shallow earthquake sources in the epicentral distance range 30–120° with Ms >5.5, correct the records for instrument response to displacement, and then remove tilt and compliance noise from the vertical component using the transfer function techniques of Crawford and Webb (2000) and Bell et al. (2015). The records are then filtered with a set of narrow band-pass filters and windowed to limit contamination with higher modes and scattered waves (Supporting Information, Figures S1 and S2). If the filtered records from an event show evidence for excessive multipathing or signal-to-noise ratios <10, those periods or stations are eliminated. In total, we use data from 107 events, well distributed in azimuth, with the number of seismograms ranging from 2,232 at 20 s to 2,910 at 50 s to 1750 at 125 s period.

3. Methods

3.1. Two-Plane Wave Method

To obtain the phase velocities as a function of azimuth, period, and location, we employed the two-plane wave method with two-dimensional finite frequency kernels (Forsyth & Li, 2005; Yang and Forsyth, 2006; Rau and Forsyth, 2011; Bell et al., 2016). Beginning with the predictions of phase velocities for an isotropic starting model, we solved for corrections to the model linearly interpolated between grid points with a 0.5° spacing. At each grid point, we assumed the phase velocity $c(f, \theta)$ as a function of frequency f and direction of propagation θ takes the form

$$c(f,\theta) = a_0(f) + a_1(f)\cos 2\theta + a_2(f)\sin 2\theta. \quad (1)$$

The 2θ terms are primarily sensitive to G_c and G_s anisotropic elastic coefficients, roughly the equivalent of azimuthal anisotropy of a horizontally traveling vertically-polarized shear wave (SV) wave (Montagner & Nataf, 1986). We neglected 4θ terms because they are expected to be small for structure with orthorhombic symmetry (Smith and Dahlen, 1973), as has been demonstrated for young seafloor near the East Pacific Rise (Weeraratne et al., 2007).

The starting isotropic phase velocity model was similar to that of Bell et al. (2016), but represented the result of iteratively inverting body and surface wave observations (VanderBeek, Forsyth, & Toomey, 2019), incorporating variations in water depth, sediment and crustal thickness, and age of the seafloor. The model was defined on a 0.5° grid, with a_0, a_1, and a_2 defined at each grid point, starting values for the a_0 terms from the Bell et al. (2016) model and starting values for a_1 and a_2 terms equal to zero to ensure that any anisotropic structure in the final model was required by the data. To obtain stable results that can be compared with the splitting results of Bodmer et al. (2015), we forced a_1 and a_2 terms to be uniform at each period for all grid points that fall into each of the four oceanic subregions illustrated in Figure 1b (i.e., describing structure that varies only in depth within each region). These regions are "JdFplate," the JdF plate interior; "JdFridge," across and immediately adjacent to the JdF, Pacific spreading center; "Blanco," adjacent to the Blanco transform fault; and "Gorda," spanning the entire Gorda plate interior and spreading ridge. The regions are selected for consistency with Bodmer et al. (2015) and group stations on a geographic basis for analysis of different tectonic regimes. We recognize that in reality, there must be anisotropic heterogeneity within each subregion, but Bodmer et al. chose the regions on the basis of relatively uniform internal *SKS* splitting

characteristics (Figure 1a), so we make the same choice in solving for averages of Rayleigh wave azimuthal anisotropy.

When using the two-plane wave method, the structure outside regions of interest is important to the measurements. To avoid bias from neglecting structure outside the subregions above, we introduced six other subregions surrounding the array in which anisotropy was also assumed to be uniform at each period. However, the anisotropic terms in those regions are poorly constrained because the limited azimuthal range possible for paths approaching the array from the outside leads to greater trade-offs with the isotropic variations; we ignore those results in the rest of this paper.

We inverted the $a_1(f)$ and $a_2(f)$ terms for perturbations to the shear velocity structure in many thin layers extending down to 410 km, with minimum length and minimum curvature regularization. The results, in terms of one particular solution to each of these non-unique problems, are shown by the dotted lines in Figures 2, 3c, and 3d for the JdF and Gorda subregions. The resolution matrices are reasonably compact with rank ~3.5, indicating that there are approximately 3.5 independent pieces of information about the anisotropic vertical structure. The average strength and direction of the fast axis can be resolved from Moho depth down to about 40 km, from 40 to 90 km, and from 90 to 210 km, with a little information about deeper structure. We expect anisotropy beneath young seafloor to develop primarily from shear strain in the evolving low-velocity zone (LVZ), so in what follows, we assume that it is negligible deeper than 210 km (Figure 4) and adopt the averages and the covariances of the three resolved layers as the starting model for a joint inversion with the splitting data.

3.2. Joint Rayleigh-*SKS* Inversion Using Monte Carlo Markov Chain

A joint inversion needs to account for the uncertainties in each method and for the strong non-linearity of shear wave splitting in the case of multiple layers with different fast directions. To address this issue, we used a Bayesian approach to simultaneously fit both data types through forward modeling. We assumed that the output of the surface wave linearized inversion forms the prior for anisotropic parameters in each of the three layers. This was parameterized as a multivariate Gaussian, inclusive of covariances between layers. We then explored model space and calculated likelihood at each point by forward modeling shear wave splitting and comparing the output to *SKS* splitting observations.

We cycled through layered anisotropic models in a Monte Carlo Markov chain, accepting or rejecting new proposed models on the basis of their relative posterior probability compared with the most recent accepted model. According to Bayes' theorem, the posterior probability of a certain model, $\mathbf{m}$, being correct given the data, $\mathbf{d}$, is proportional to the product of a prior probability and a likelihood term:

$$p(\mathbf{m}|\mathbf{d}) \propto p(\mathbf{m})\, p(\mathbf{d}|\mathbf{m}), \tag{2}$$

where $p(\mathbf{m})$ is the multivariate Gaussian prior distribution from the surface wave inversion, and the likelihood term, $p(\mathbf{d}|\,\mathbf{m})$, is defined below.

The proposed models were created by normally perturbing sine and cosine anisotropic terms from the most recently accepted model (one pair of terms per layer). Proposal distributions were chosen to achieve ~50% model acceptance, balancing exploration (trying new regions of model space) and investigation (assessment proximal to a locality of model space). These models were used to forward model *SKS* splitting by propagating synthetic pulses through each anisotropic model, as follows: for each layer, we calculated the full anisotropic tensor by assuming orthorhombic A-type fabric (e.g., Ismaïl & Mainprice, 1998) using a scaled version of the tensor computed for olivine by Anderson (1989), with horizontal a- and b-axes. We also tested using a hexagonal fabric with horizontal symmetry axis in the a-direction. In each iteration, the tensors are scaled to that model's horizontal shear wave anisotropy. The approach of using a simply scaled tensor to reduce the anisotropic parameter space has been validated elsewhere in anisotropic tomography studies (e.g., Abt & Fischer, 2008; Mondal & Long, 2019).

Synthetic input waveforms comprised a 5-s Gaussian pulse on the radial component and zero energy on the transverse component, with random white noise then added for a signal-to-noise ratio of 5 on the radial component. Forward modeling entailed the propagation of these synthetic pulses through the layered model structure using source parameters and back azimuths for the 16 most commonly observed earthquakes in

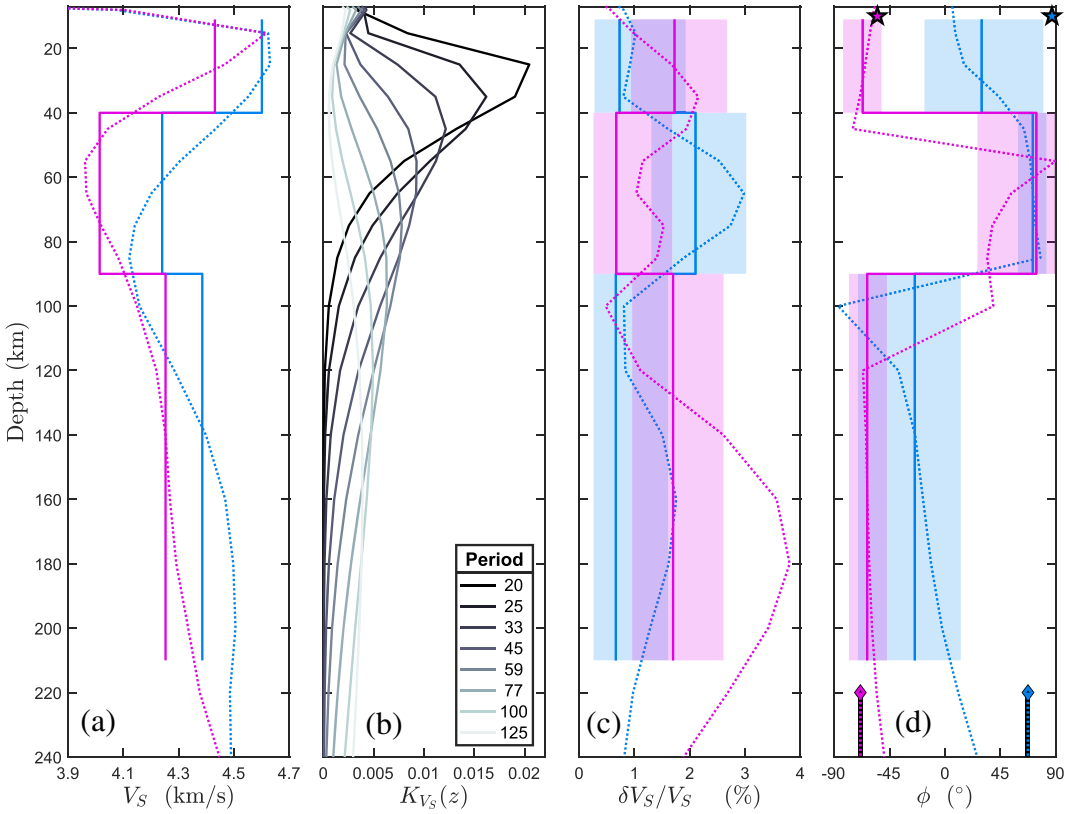

Figure 4. Vertical profiles of seismic structure from immediately below the crust (11 km) down to 240-km depth. Panels show (a) shear velocity structure; (b) anisotropy sensitivity kernels; (c) amplitude of azimuthal anisotropy as a fraction of shear velocity; and (d) anisotropic fast azimuth. All profiles in (a, c, d) show results from linearized inversion of Rayleigh wave data alone (section 4); dotted lines are from a finely discretized inversion and solid lines show values averaged into three layers that data importance values indicate are independently resolvable. Shaded regions indicate 95% uncertainties. The Juan de Fuca profile is in blue and Gorda in pink, as in Figure 1. Stars denote average *Pn* measurements for the two plate interiors (VanderBeek & Toomey, 2017, 2019). Lines with diamonds at the bottom show mean *SKS* splitting observations in these regions (Bodmer et al., 2015).

the data set employed by Bodmer et al. (2015), computing ray parameters using the 1D IASP91 model. We solved the Christoffel equations for fast and slow *S* wave propagation velocities and polarizations in each layer in a ray-based coordinate system. Taking each layer in series, seismograms were rotated into fast/slow polarization and delayed by the appropriate splitting time. Finally, we output virtual north and east components, corresponding to an "observation" at the top of the model.

The resultant synthetic data were "unsplit" using the average splitting parameters observed in the Bodmer study for each of the study regions (Figure 1), rotating and shifting pulses according to the (single layer) splitting time (δt) and fast azimuth (φ) measured in that study. In reference to the "minimum energy" method of Silver and Chan (1991), the transverse component energy, E_T, was used to define a misfit term that dictated the *likelihood* of this data having been observed *given* the proposed model:

$$p(\mathbf{d}|\mathbf{m}) = exp\left(-\frac{\sum_i E_{T_i}}{\gamma^2}\right), \tag{3}$$

where E_T was calculated as the root mean square (RMS) of the "unsplit" transverse component divided by the RMS of the "split" transverse component, within the 9-s window extending 2 s on either side of the original radial component signal. γ is a misfit penalty weighting, discussed below. Thus, if a proposed model yielded synthetic splitting highly consistent with that observed by Bodmer et al. (2015), then the "unsplit" transverse would have contained very little energy, and the likelihood probability would have been high.

The proposed models were accepted (replacing the current model) or rejected using a Metropolis-Hastings acceptance criterion (Hastings, 1970; Metropolis & Rosenbluth, 1953):

$$p_{\text{accept}} = \left\lceil \min\left(\frac{p(\mathbf{m}_1)p(\mathbf{d}|\mathbf{m}_1)}{p(\mathbf{m}_0)p(\mathbf{d}|\mathbf{m}_0)}, 1\right) \geq r \right\rceil, \tag{4}$$

where $\mathbf{m}_0$ is the current model, $\mathbf{m}_1$ is the proposed model, and r is a number between 0 and 1 randomly generated from a uniform distribution. We ran 14 individual chains with 10^5 inversions per chain, saving the current model every 100 iterations. The concatenated ensemble of saved models yielded the empirical posterior model distribution: anisotropic strengths and fast axis orientations in each of the three modeled layers. The posterior was compared with the empirical prior, which was the ensemble generated by running the inversion without splitting data (i.e., with likelihood set to unity) that reflects the surface wave constraints alone.

In order to compare the results from the Bayesian inversion directly with the observed splitting, we selected 500 models at random from the ensemble of accepted models. For each of these 500 models, we computed synthetic splitting as described above, using 16 input events at a range of back azimuths per model. The resultant split traces were then inverted using the minimum energy method (Silver & Chan, 1991) to obtain single-layer δt and φ values. We stacked the error surfaces (i.e., the unsplit transverse component energy at each combination of δt and φ) across all events for all 500 sampled models.

The parameter γ is key to determining the behavior of this inversion. If γ is large ($\gamma > 5$), substantial energy on the transverse component barely affects the likelihood, and the posterior distribution tends towards the prior, emphasizing the surface wave constraints. If γ is small ($\gamma < 0.1$), then even modest transverse energy substantially diminishes the likelihood term, and the posterior distribution ignores the prior, instead fitting only the *SKS* splitting constraints (and frequently getting stuck in local misfit minima). We conducted L-testing to determine γ values that required the inversion to simultaneously fit both data types well and report inversions using $\gamma = 2$.

4. Results

4.1. Rayleigh Wave Phase Velocity Inversion

The JdF and Gorda regions are substantially better resolved than other subregions and thus are the focus of our analysis. The mean standard deviations in anisotropic amplitude are 6.0 and 7.5 m/s, respectively, corresponding to average two-sigma errors in fractional anisotropy of 0.37% and 0.52%. Of the 15 periods studied, almost all show anisotropy values statistically significantly discernible from zero at 95% confidence in these two subregions; the exceptions are long periods at JdF, which have well-resolvedly small values.

Isotropic shear velocity profiles for these regions are similar, both exhibiting a fast lithospheric lid, a clear LVZ, and then a gradual increase in shear velocity with depth (Figure 4a). Consistent with the JdF's greater average age, its lid is thicker, ~40 versus ~20 km for Gorda. This is roughly consistent with *S-p* estimates of the negative velocity gradient (Rychert et al., 2018) and other surface wave studies (Gao, 2016). The Gorda LVZ is ~0.20 km/s slower than that beneath the JdF (3.95 vs. ~4.15 km/s), which is not obviously predicted by differences in mean plate age (note that the Gorda region includes the spreading center but the JdF does not), but is consistent with previous observations from teleseismic body waves (Byrnes et al., 2017; Eilon & Abers, 2017) and the inference of downwelling beneath the interior of the JdF plate.

Even prior to inversions, patterns of $a_1(f)$ and $a_2(f)$ terms reveal a clear frequency-dependent variation in azimuthal anisotropy (Figures 2, 3, S3, S4a, and S4b). This signal is well resolved and shows very little trade-off with other subregions or with the isotropic (a_0) terms that are allowed to vary on the 0.5° scale. Converting a_1 and a_2 to amplitude and fast direction (Figures 2, 3, S3, S4c, and S4d) shows that peak-to-peak amplitude is generally on the order of 2% and that fast directions are relatively consistent within each subregion, particularly at periods of 50 s or less. Plotting histograms of the fast directions in all four oceanic subregions at periods ≤50 s (Figure 1b) shows that, at these periods, the Rayleigh wave anisotropy is clearly related to the anisotropy detected in *SKS* splitting, with fast direction ENE in the JdF region and ESE in the Gorda and Blanco regions. As with the *SKS* splits, there is no consistent direction for the vicinity of the JdF ridge. Qualitatively, there is a reduction in strength of azimuthal anisotropy at periods greater than 50 s in the

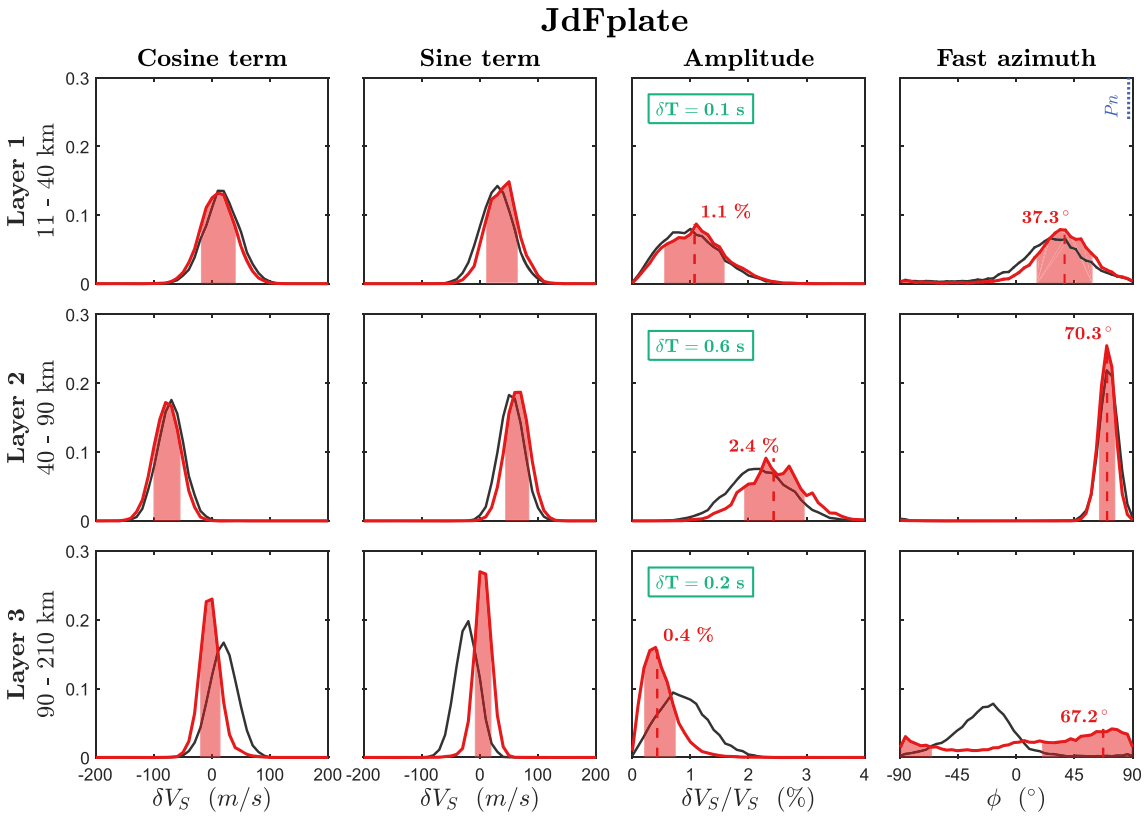

Figure 5. Results of joint inversions for anisotropic parameters in the three well-resolved layers for the JdFplate region. Left two columns show coefficients of azimuthal anisotropy in units of m/s and right two columns show fractional amplitude and fast azimuth of anisotropy. Black curves are empirical prior distributions, red curves show posterior distributions accounting for fit to shear wave splitting data, with median values of amplitude and fast azimuth given, and ±1 standard deviation regions shaded in light red. The *Pn* fast azimuth, shown in blue, is from VanderBeek and Toomey (2017). Green text gives predicted splitting time (δT) accumulated within each layer (although fast axis orientation differences mean that times are not straightforwardly additive).

JdF region (Figure 2c), suggesting either a reduction in strength of the anisotropy with increasing depth or a change in direction that interferes with the shallow anisotropy at the longer periods that average over a greater depth range.

Our inversions illustrate in detail the differences in anisotropic structure between the subregions. Taking the non-unique detailed anisotropy depth profiles of the starting model at face value (dotted lines, Figure 4), the JdF region is characterized by strong shallow anisotropy with ENE-WSW fast axis orientation. This anisotropy is strongest (~2.5%) in the depth range corresponding to the LVZ. Gorda, which is dominated by ESE-WNW fast azimuths, has modest anisotropy in the upper mantle, with a similar minimum amplitude displaced ~40 km deeper than the LVZ and a local maximum at the top of the LVZ. Unexpectedly, the strongest Gorda anisotropy (up to ~3.5%) is observed at depths of ~180 km.

4.2. Bayesian Joint Inversions

Resolution analysis (section 4) leads us to place more confidence in the average structures found for the three layers used for the Bayesian joint inversion, that is, 11- to 40-, 40- to 90-, and 90- 210-km depth (Figures 4c and 4d). The probability distributions for each layer in each region are shown in Figures 5, 6, S5 and S6 with summarized results in Table 1. About 53.5% of models in the post-burn-in Markov chain Monte Carlo (MCMC) were accepted, demonstrating an efficient exploration of parameter space with appropriately chosen proposal distribution. We found that the assumption of the fabric type did not matter; "A-type" orthorhombic and "tilted transverse isotropic" hexagonal fabrics gave indistinguishable results, perhaps unsurprisingly given that horizontal fast and slow shear velocities are scaled similarly in each case.

The JdF fast direction is 37 ± 40° (95% confidence intervals are quoted here and below) in the uppermost layer, rotating clockwise in the middle layer to 70 ± 11°. At depths greater than ~90 km, the JdF

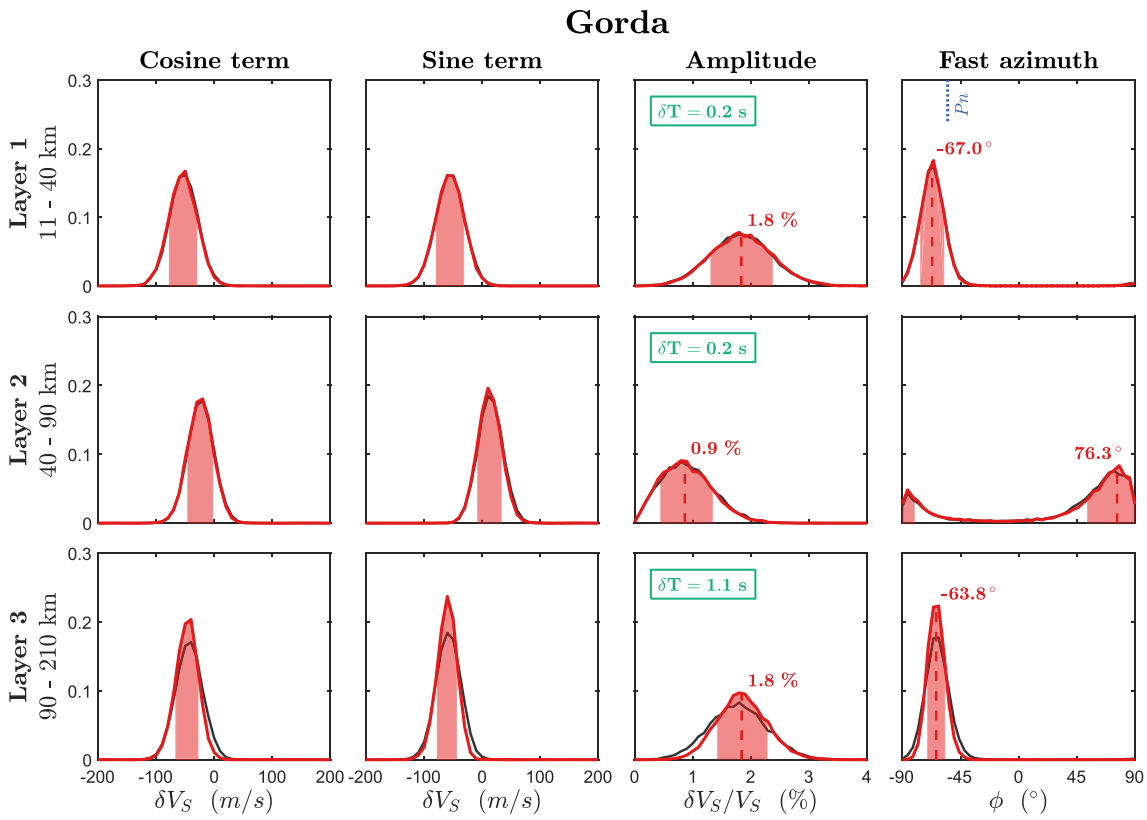

Figure 6. As for Figure 5, but showing results from the Gorda region. The *Pn* result is from VanderBeek and Toomey (2019).

anisotropy becomes too weak (<0.5%) to clearly constrain; our Bayesian inversion shows that while the surface wave data weakly constrain it to be SSE-NNW fast, there is no significant loss of data fit with essentially null deep anisotropy here. The Gorda region has stronger (~1.8%) anisotropy in the top and bottom layers, with weaker anisotropy (~0.9 ± 0.7%) in the LVZ depth range from 40 to 90 km. The fast azimuth in the well-constrained layers within the Gorda region is ~115 ± 16°.

The error maps based on forward computations from models in the Bayesian final ensemble (Figures 7 and S7) show the overall energy minimum as well as average splitting parameters reported by Bodmer et al. (2015) in each region. The close agreement in overall splitting parameters demonstrates the fundamental compatibility of the surface wave and *SKS* measurements; our final models fit both data sets well.

Table 1
Layered Anisotropy in Each Subregion

Region	Depth range (km)	Amplitude (%)	Azimuth
JdFplate	11–40	1.1 ± 0.5	37° ± 21.4
	40–90	2.4 ± 0.5	70° ± 6.1
	90–210	0.4 ± 0.3	67° ± 47.2
Gorda	11–40	1.8 ± 0.5	113° ± 9.1
	40–90	0.9 ± 0.4	76° ± 23.0
	90–210	1.8 ± 0.4	116° ± 6.7
Blanco	11–40	1.2 ± 0.7	98° ± 38.2
	40–90	1.6 ± 0.7	120° ± 15.1
	90–210	0.9 ± 0.5	101° ± 21.7
JdFridge	11–40	1.2 ± 0.7	124° ± 45.8
	40–90	1.3 ± 0.7	103° ± 32.5
	90–210	2.0 ± 0.7	29° ± 11.5

Note. Summary of joint inversion results for anisotropy strength and direction in each subregion. Mean values are given, with 68th percentile (~1σ) uncertainty bounds indicated.

4.3. Less Well-Resolved Regions: Blanco and the JdF Ridge Axis

As mentioned above, our emphasis is on the best resolved JdF plate interior and Gorda regions, but we also conducted analyses using the smaller subsets of stations on the JdF ridge and Blanco transform fault subregions (Figure 1). We consider the latter two regions less well resolved because the error bars on the separate $a_1(f)$ and $a_2(f)$ coefficients are larger—these subregions have mean standard deviations in anisotropic amplitude terms of 9.1 and 12.4 m/s, respectively (Figures S3a, S3b, S4a, and S4b), although the Rayleigh wave fast direction for Blanco is quite consistent, particularly at periods of 50 s and less (Figures 1b and S3d). These uncertainties correspond to 0.66% and 0.93% two-sigma values of fractional anisotropy; at

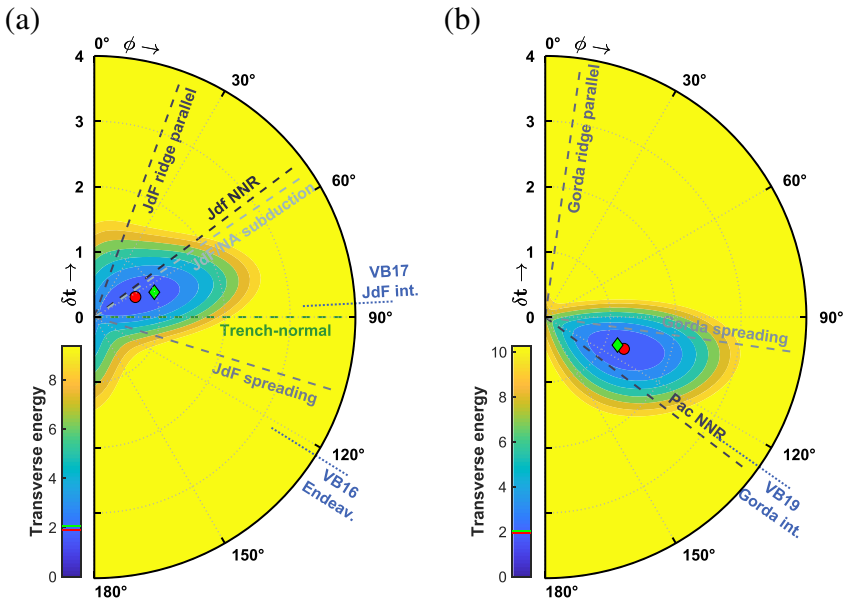

Figure 7. Stacked misfit surface for splitting parameters calculated by forward modeling additive splitting through 500 models selected randomly from the posterior ensemble of acceptable models for the Juan de Fuca (a) and Gorda (b) subregions. Radial distance corresponds to splitting time (δt, in seconds) and angle corresponds to fast azimuth (φ) assuming a 2θ pattern. The misfit is computed according to minimum energy method (Silver & Chan, 1991). Red dot: minimum of misfit surface; green diamond: mean splitting parameters computed by (Bodmer et al., 2015) averaged over the region. Red and green lines on color bar show relative energy of these points. Various dynamically relevant directions are overlaid: "NNR" is APM in the no-net-rotation frame, "Pac" is the Pacific plate, "JdF" is Juan de Fuca, NAm is North America, and VB is (Vanderbeek et al., 2016; VanderBeek & Toomey, 2017, 2019) *Pn* fast directions.

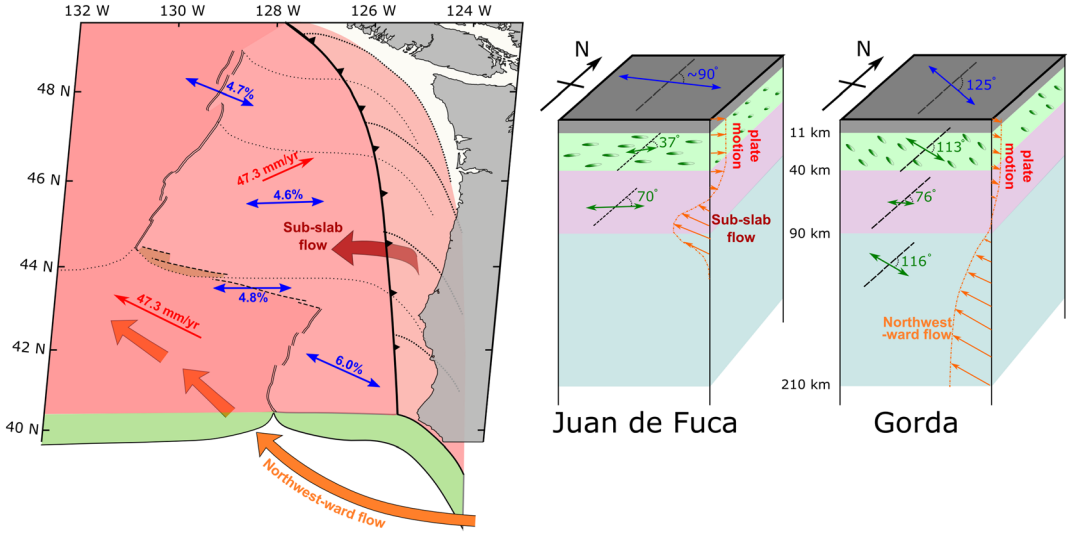

Figure 8. Cartoon of 3-D mantle flow beneath study area, with flow and measured anisotropy in average 1-D columns beneath the Juan de Fuca and Gorda plate regions. Northwestward flow around the slab edge (yellow) and subslab return flow (red) processes are marked. The green icons in the columns represent lithospheric fabric. Fast directions are defined in degrees clockwise from north; green arrows indicate mantle structure measured by surface and *SKS* waves and blue arrows indicate *Pn* measurements.

many periods, we cannot statistically differentiate the anisotropic terms from zero. Larger uncertainties are unsurprising in these regions, both of which are small, include relatively few stations, and contain plate boundaries that may have particularly strong gradients in structural anisotropy. In both regions, measured *SKS* fast directions are also more variable than in the Gorda and JdF plate subregions (Figure 1a).

Nonetheless, taken at face value, the results in the two less well-resolved regions also demonstrate depth-dependent structure and heterogeneity between subregions. Within the vicinity of the Blanco transform fault (Figure S5), the joint inversion indicates more vertically continuous structure with φ roughly WNW-ESE. This direction approximates the strike of the transform. The strength of anisotropy seems to slightly decrease in the deepest layer we inverted, although the trend is not statistically significant. On the JdF ridge itself (Figure S6), ~1.2% anisotropy in the 11- to 40-km depth range has φ ~124°, subparallel to spreading direction and in close agreement with *Pn* direction, although much weaker. VanderBeek et al. (2016) measured 4.7% *P* anisotropy immediately beneath the Moho in the northern part of the ridge. Interestingly, our data indicate that φ changes to ~30° at depths of 90–210 km in this region.

5. Discussion and Conclusions

5.1. Comparison with *SKS*

Our forward modeling (Figure 7) demonstrates that Rayleigh wave azimuthal anisotropy measurements are compatible with *SKS* observations. In an improvement over *SKS* data alone, we observe substantial depth dependency to the anisotropic structure in the regions that are best resolved in our study. Notably, the deep structure is clearly decoupled from the surface geology. On the basis of isotropic velocity profiles, and our prior expectations for young oceanic thermal structure, we interpret depths <40 km as the lithospheric lid, 40–90 km as the lowest velocity and viscosity asthenosphere, and 90- to 210-km depth as the underlying convecting mantle or deeper asthenosphere.

5.2. Comparison with *Pn*

We observe uneven consistency between *Pn*-derived fast axes and the fast directions in the shallowest layer of our inversions. In the Gorda region, anisotropic fast directions in our lithospheric lid are indistinguishable from measured *Pn* phase data given reported uncertainties; we observe φ ~113° and VanderBeek and Toomey (2019) report an average value of $\varphi = 116 \pm 6°$. On the other hand, within the interior of the JdF plate, our inversion suggests φ = ~40° in the uppermost layer, which is at a high angle to *Pn* measurements of $\varphi = 87 \pm 3°$ in the JdF interior or $\varphi = 122 \pm 1°$ on the (Endeavour) ridge axis (VanderBeek et al., 2016; VanderBeek & Toomey, 2017). Although the JdF region's lithospheric anisotropy is weaker (~1.1%) and less well azimuthally resolved ($\pm$40° at 95% confidence) than in the Gorda subregion (strength ~1.8%, with ~16° uncertainty in azimuth), it is not straightforward to reconcile our values with the highly precise *Pn* data.

Pn phases travel in the upper 10 km (or less) of the mantle, a depth range to which our ≥20-s Rayleigh waves do not have much sensitivity (Figure 4). Thus, it is not physically incompatible for these measurements to differ. Rather, the data seem to imply strong gradients in anisotropic structure between 10-km depth (roughly where *Pn* is most sensitive) and ~25-km depth (the center of our upper layer and maximum sensitivity of 20-s Rayleigh waves here), although we cannot place tight depth constraints on exactly how this gradient is distributed within the upper layer. Uppermost mantle fabrics that dominate *Pn* anisotropy are likely responding to a combination of shear associated with shallow corner flow driven by plate separation and shear associated with motion relative to deeper mantle in the vicinity of the ridge (Blackman et al., 2002; Castelnau et al., 2009; Toomey et al., 2007; VanderBeek et al., 2016; Wolfe & Solomon, 1998). We also note that both surface wave and *Pn* measurements in the JdF interior involve spatial averaging over hundreds of kilometers. Part of the discrepancy in fast azimuths could arise from a combination of strong horizontal gradients in shallow anisotropy and different regions of sensitivity between the two data sets. Finally, differences in measured strength might relate to olivine having larger intrinsic fractional *P* wave anisotropy than *S* wave anisotropy.

5.3. Lithospheric Anisotropy

There is notable mismatch between the JdF "lithospheric" fast direction we observe (φ ~40°) and the direction of plate spreading (~120°) (Figure 7). Paradoxically, our measurements indicate a clockwise rotation of fast axes with increasing depth in this region (Figure 2d), opposite to what one would expect if shallowmost

structures were controlled by ridge processes and deeper structure by plate motion. It is difficult to construe how APM could account for these observations: the lithospheric fabric is even further anticlockwise from spreading than APM (~50°). Our measurement disagrees with some models (e.g., Blackman et al., 2002) and observations at fast ridges (e.g., Wolfe & Solomon, 1998) but is more consistent with measurements in slow spreading ocean basins (Becker et al., 2014). At 50 mm/yr full spreading rate, the JdF is a medium-slow spreading ridge. Several other regional studies have found substantial rotation of oceanic lithosphere fabric away from the spreading direction, for instance at the mid-Atlantic ridge (38° off) (Dunn et al., 2005), in 60-Ma Pacific seafloor (~55° off) (Takeo et al., 2016) and in 140-Ma Pacific seafloor (70° off) (Takeo et al., 2018). Our work adds to this canon and should inform models of subridge fabric build up at low strain rates. In this context, however, it is then interesting that the Gorda region—also formed at ~40–50 mm/yr (Wilson, 1989)—should have shallow anisotropy so closely aligned with the local spreading direction. Most likely, this is induced by vertical rotation axis shear distributed across much of the Gorda plate that accommodates motion between Pacific and JdF plates (Chaytor et al., 2004; Wilson, 1989, 1993).

A number of studies have argued for dynamic upwelling and associated off-axis downwelling at the JdF ridge axis, on the basis of attenuation (Eilon & Abers, 2017; Ruan et al., 2018), mantle LVZ morphology (Byrnes et al., 2017), and a rapid increase in shear velocity with age to depths greater than predicted by purely conductive cooling. It may be that in the JdF plate interior, downwelling of the mantle near the ridge axis has disrupted the expected continuation of spreading-parallel anisotropy to the deeper lithosphere. This downwelling is not expected at the shallower depths traversed by *Pn* phases. The rapid shear velocity increase observed beneath the JdF plate is not seen beneath the Gorda plate. This lack of obvious downwelling may explain why Gorda evinces the more predictable ridge-perpendicular anisotropy to greater depth. Sheared melt structures can also cause azimuthal anisotropy (cf. Beghein et al., 2014; Holtzman et al., 2003) but with a fast axis aligned perpendicular to flow direction. In both Gorda and JdF regions, it is possible that >20 km deep residual melt pockets suggested by modeling (Keller et al., 2017) align to yield a shape-preferred orientation fabric that complicates simple CPO-dominated anisotropy by introducing a spatially discontinuous flow-perpendicular fast axis in regions of more melt.

The evident possibility for complex ridge dynamics to interrupt simple corner flow-motivated models is of import to global understanding of oceanic fabric development. The spreading-parallel *SKS* splitting seen in the Mantle Electromagnetic and Tomography (MELT) region of the East Pacific Rise (Wolfe & Solomon, 1998) increasingly seems like an exception, rather than a rule. Our data suggest that a simple conceptualization of spreading-parallel fabric "fossilized" into the oceanic lithospheric from formation at the ridge is incorrect. More regional studies in the oceans are clearly required to investigate this phenomenon and its plausible relationship to spreading rate.

5.4. Sublithospheric Anisotropy

Beneath the JdF region, the strongest anisotropy is oriented 70° ± 10° and concentrated in the 40- to 90-km depth range, which is the zone of lowest shear wave velocities and presumably lowest viscosities. The simplest explanation for strong anisotropy at this depth is shear-generated CPO between the lithosphere and the convecting mantle. While this feature is not formally resolvable, the full profiles (Figure 4, dashed lines) show that maximum anisotropy strength is at the upper edge of the LVZ, similar to the findings of Lin et al. (2016) and also to global observations of radial anisotropy (Moulik et al., 2019), and the lowest anisotropy amplitude is found ~30 km deeper than the LVZ center. We are cautious of overinterpreting this feature given the poor depth resolution, but it is consistent with strain localization towards the boundaries of a low-viscosity channel with non-linear rheology.

The isotropic shear velocities beneath the plates are low for both regions (~4.15 km/s for the JdF interior and ~3.95 km/s for Gorda). These values likely require the presence of partial melt, which can result in substantial anisotropy, including an azimuthal component if there are horizontal shear or permeability gradients (Holtzman et al., 2003). However, sheared melt is a poor explanation for observed sublithospheric anisotropy, as the associated flow-perpendicular fast axes would require flow fields that would here need to be aligned highly oblique to plate motion. Similarly, aligned pockets of melt ponded at a sublithospheric compaction boundary (or similar) are predicted to yield a fast fabric parallel to magnetic lineations (Holtzman & Kendall, 2010), inconsistent with our observations in the plate interior.

The fast direction within the JdF is oriented approximately parallel to APM (53°; Kreemer et al., 2014; Figure 1), but the direction is rotated ~20° clockwise by westward-directed return flow towards the ridge (Figure 8), driven by plate rollback (Eakin et al., 2010; Zandt & Humphreys, 2008), and/or subslab return flow of buoyant material suggested by seismic and geodetic data (Bodmer et al., 2018; Hawley et al., 2016). This deep return flow likely enhances the net shear in this depth range, as top flows NE while bottom moves W, explaining the largest amplitude of well-resolved anisotropy that we report (2.4 ± 0.8%). At depths of 90–210 km, the JdF plate interior has essentially no discernible anisotropy.

Beneath the Gorda region, anisotropy is strongest (~1.8 ± 0.6%) deeper than 90 km. The fast azimuth (116 ± 8°) is strikingly consistent with the lithospheric fabric (~113°), but given the negligible intermediate layer anisotropy, a physical linkage between the two layers is conceptually challenging to justify. Rather, this well-constrained deep anisotropy results from flow around the southern end of the subducting plate (Figure 8), part of global flow pattern partly driven by motion of the Pacific plate, which aligns approximately with the fast direction we see. Dynamical modeling (Zhou et al., 2018) predicts that return flow around the slab edge coupled with large-scale entrainment by the Pacific plate should produce strong WNW-ESE fabrics at >100-km depth beneath Gorda. The exact directions are somewhat contingent on the boundary conditions of the models, but generally hold. The same models indicate much more disorganized or weak fabric at 100- to 300-km depth beneath the JdF plate proper, in agreement with our finding of negligible deep anisotropy in this region. This arises because the subducted Farallon/JdF plate acts as a barrier to large-scale Pacific-dominated flow to the NW, and so the upper mantle seaward of the slab is in a flow shadow (Figure 8).

At depths of 40–90 km, the Gorda region has relatively modest anisotropy, despite the presence of a low-velocity and (presumably) low-viscosity layer. We posit that this results from limited differential shear between Gorda and the underlying mantle, as deformation of the Gorda plate is driven by shallow, direct, plate-plate interaction with the Pacific plate (Wilson, 1989, 1993) and the Pacific plate dominates local convecting mantle flow. We note that this would be the opposite scenario to the other end of the JdF plate system, where the Explorer plate seems to have been captured by North America, with almost complete decoupling from underlying mantle flow (Mosher et al., 2014). The limited (0.8 ± 0.7%) anisotropy at 40–90 km beneath Gorda may also simply reflect the young plate age: insufficient strain or the imprint of a prior fabric would both result in a weak CPO record of differential motion here (cf. Boneh et al., 2015; Boneh & Skemer, 2014; Kaminski & Ribe, 2002).

5.5. Ridge and Transform Regions

In light of poor resolution, especially at depth within the aperture-limited JdF ridge and Blanco transform mini arrays, we hesitate to overinterpret the structure modeled in these regions. However, we note that in both cases, the orientation of shallow anisotropy conforms well with prior expectations for the respective structures: spreading parallel at the ridge and fault parallel on the transform. These structures also yield splitting predictions close to the observed *SKS* results (Bodmer et al., 2015; Martin-Short et al., 2015). If the deepest layer below the JdF ridge is to be believed, there is an intriguing rotation of fast axis here from spreading parallel at depths <90 km (presumably due to strain-related CPO) to ridge parallel at depths >90 km. If the deep structure is real, it likely results from predominantly vertical flow and possibly aligned melt lenses oriented perpendicular to minimum compressive stress; melt at this depth is consistent with a deep channel of high attenuation (Eilon & Abers, 2017) and may drive dynamic upwelling.

5.6. Summary

Our shorter-period data can be explained by a model involving a Gorda plate with strong lithospheric anisotropy presumably generated by MOR processes and internal strain (Gaherty, 2004; VanderBeek & Toomey, 2019) and weak intermediate depth anisotropy due to diminished or recently extinct shear over underlying mantle. The JdF region has weak lithospheric anisotropy, but a strong asthenospheric fabric caused by motion of the plate in combination with local mantle flow fields. At depths associated with the convecting mantle (>90 km), substantial anisotropy is observed in the Gorda region, possibly associated with regional mantle flow fields interacting with the Farallon slab; the weakness of fabric at depth beneath the JdF plate may imply that this region is in the flow shadow of the slab.

Data Availability Statement

All waveform data used for this study are openly available through the IRIS Data Management Center (https://ds.iris.edu/ds/nodes/dmc/) under network codes 7D (Cascadia Initiative Community Experiment), X9 (Blanco Transform), and TA (Transportable Array). Results from this study are archived via Dryad at https://doi.org/10.25349/D9N01T, and prior results quoted are available in Bodmer et al. (2015) and Bell et al. (2016).

Conflict of Interest

The authors declare that they have no conflicts of interest pertaining to this work.

Acknowledgments
We gratefully recognize the many individuals who enabled the Cascadia Initiative community seismic experiment, in particular the ship operators, SIO, LDEO, and WHOI OBSIP Instrument Centers, cruise volunteers, and PIs. We acknowledge the contributions of Youyi Ruan and Samuel Bell in assisting with the processing of surface wave data from this deployment. This work is funded by NSF grants OCE-1658214 (ZE), EAR-1547368 (DF), and OCE-1332876 (DF).

References

Abt, D. L., & Fischer, K. M. (2008). Resolving three-dimensional anisotropic structure with shear wave splitting tomography. *Geophysical Journal International*, *173*(3), 859–886. http://doi.org/10.1111/j.1365-246X.2008.03757.x

Anderson, D. L. (1989). Theory of the Earth: Chapter 15—Anisotropy. In *Theory of the Earth* (pp. 1–34).

Auer, L., Becker, T. W., Boschi, L., & Schmerr, N. (2015). Thermal structure, radial anisotropy, and dynamics of oceanic boundary layers. *Geophysical Research Letters*, *42*(22), 9740–9749. https://doi.org/10.1002/2015GL066246

Auer, L., Boschi, L., Becker, T. W., Nissen Meyer, T., & Giardini, D. (2014). Savani: A variable resolution whole-mantle model of anisotropic shear velocity variations based on multiple data sets. *Journal of Geophysical Research: Solid Earth*, *119*, 3006–3034. https://doi.org/10.1002/2013JB010773

Becker, T. W., Conrad, C. P., Schaeffer, A. J., & Lebedev, S. (2014). Origin of azimuthal seismic anisotropy in oceanic plates and mantle. *Earth and Planetary Science Letters*, *401*, 236–250. https://doi.org/10.1016/j.epsl.2014.06.014

Becker, T. W., Kustowski, B., & Ekström, G. (2008). Radial seismic anisotropy as a constraint for upper mantle rheology. *Earth and Planetary Science Letters*, *267*(1–2), 213–227. https://doi.org/10.1016/j.epsl.2007.11.038

Becker, T. W., and S. Lebedev (2019). Dynamics of the lithosphere and upper mantle in light of seismic anisotropy,

Beghein, C. (2018). Thermal nature and resolution of the lithosphere-asthenosphere boundary under the Pacific from surface waves,

Beghein, C., Yuan, K., Schmerr, N., & Xing, Z. (2014). Changes in seismic anisotropy shed light on the nature of the Gutenberg discontinuity. *Science*, *343*(6176), 1237–1240. https://doi.org/10.1126/science.1246724

Bell, S., Ruan, Y., & Forsyth, D. W. (2016). Ridge asymmetry and deep aqueous alteration at the trench observed from Rayleigh wave tomography of the Juan de Fuca plate. *Journal of Geophysical Research: Solid Earth*, *121*, 7298–7321. https://doi.org/10.1002/2016JB012990

Bell, S. W., Ruan, Y., & Forsyth, D. W. (2015). Shear velocity structure of abyssal plain sediments in Cascadia. *Seismological Research Letters*, *86*(5), 1247–1252. https://doi.org/10.1785/0220150101

Blackman, D. K., Wenk, H. R., & Kendall, J. M. (2002). Seismic anisotropy of the upper mantle 1. Factors that affect mineral texture and effective elastic properties. *Geochemistry, Geophysics, Geosystems*, *3*(9), 8601. https://doi.org/10.1029/2001GC000248

Bodmer, M., Toomey, D. R., Hooft, E. E., Nábělek, J., & Braunmiller, J. (2015). Seismic anisotropy beneath the Juan de Fuca plate system: Evidence for heterogeneous mantle flow. *Geology*, *43*, 1–5. https://doi.org/10.1130/G37181.1

Bodmer, M., Toomey, D. R., Hooft, E. E. E., & Schmandt, B. (2018). Buoyant asthenosphere beneath Cascadia influences megathrust segmentation. *Geophysical Research Letters*, *45*, 6954–6962. https://doi.org/10.1029/2018GL078700

Boneh, Y., Morales, L. F. G., Kaminski, E., & Skemer, P. (2015). Modeling olivine CPO evolution with complex deformation histories: Implications for the interpretation of seismic anisotropy in the mantle. *Geochemistry, Geophysics, Geosystems*, *16*, 3436–3455. https://doi.org/10.1002/2015GC005964

Boneh, Y., & Skemer, P. (2014). The effect of deformation history on the evolution of olivine CPO. *Earth and Planetary Science Letters*, *406*, 213–222. https://doi.org/10.1016/j.epsl.2014.09.018

Boneh, Y., Wallis, D., Hansen, L. N., Krawczynski, M. J., & Skemer, P. (2017). Oriented grain growth and modification of "frozen anisotropy" in the lithospheric mantle. *Earth and Planetary Science Letters*, *474*, 368–374. https://doi.org/10.1016/j.epsl.2017.06.050

Braun, M. G., Hirth, G., & Parmentier, E. M. (2000). The effects of deep damp melting on mantle flow and melt generation beneath mid-ocean ridges. *Earth and Planetary Science Letters*, *176*, 339–356. https://doi.org/10.1016/S0012-821X(00)00015-7

Byrnes, J. S., Toomey, D. R., Hooft, E. E. E., Nábělek, J., & Braunmiller, J. (2017). Mantle dynamics beneath the discrete and diffuse plate boundaries of the Juan de Fuca plate: Results from Cascadia Initiative body wave tomography. *Geochemistry, Geophysics, Geosystems*, *15*, 3521–3524. https://doi.org/10.1002/2017GC006980

Castelnau, O., Blackman, D. K., & Becker, T. W. (2009). Numerical simulations of texture development and associated rheological anisotropy in regions of complex mantle flow. *Geophysical Research Letters*, *36*, L12304. https://doi.org/10.1029/2009GL038027

Chaytor, J. D., Goldfinger, C., Dziak, R. P., & Fox, C. G. (2004). Active deformation of the Gorda plate: Constraining deformation models with new geophysical data. *Geology*, *32*(4), 353–356. http://doi.org/10.1130/G20178.1

Crawford, W. C., & Webb, S. C. (2000). Identifying and removing tilt noise from low-frequency (<0:1 Hz) seafloor vertical seismic data. *Bulletin of the Seismological Society of America*, *90*, 952–963.

Debayle, E., & Ricard, Y. (2013). Seismic observations of large-scale deformation at the bottom of fast-moving plates. *Earth and Planetary Science Letters*, *376*, 165–177. https://doi.org/10.1016/j.epsl.2013.06.025

Dunn, R. A., Lekić, V., Detrick, R. S., & Toomey, D. R. (2005). Three-dimensional seismic structure of the mid-Atlantic ridge (35°N): Evidence for focused melt supply and lower crustal dike injection. *Journal of Geophysical Research*, *110*, B09101. http://doi.org/10.1029/2004JB003473

Eakin, C. M., Obrebski, M., Allen, R. M., Boyarko, D. C., Brudzinski, M. R., & Porritt, R. (2010). Seismic anisotropy beneath Cascadia and the Mendocino triple junction: Interaction of the subducting slab with mantle flow. *Earth and Planetary Science Letters*, *297*(3–4), 627–632.

Eakin, C. M., Rychert, C. A., & Harmon, N. (2018). The role of oceanic transform faults in seafloor spreading: A global perspective from seismic anisotropy. *Journal of Geophysical Research: Solid Earth*, *123*, 1736–1751. https://doi.org/10.1002/2017JB015176

Eddy, C. L., Ekström, G., & Journal, M. N. G. (2018). Age dependence and anisotropy of surface-wave phase velocities in the Pacific. *Geophysical Journal International*, *216*(1), 640–658. https://doi.org/10.1093/gji/ggy438

Eilon, Z. C., & Abers, G. A. (2017). High seismic attenuation at a mid-ocean ridge reveals the distribution of deep melt. *Science Advances*, *3*, e1602829.

Eilon, Z. C., Abers, G. A., Jin, G., & Gaherty, J. B. (2014). Anisotropy beneath a highly extended continental rift. *Geochemistry, Geophysics, Geosystems*, *15*, 545–564. https://doi.org/10.1002/2013GC005092

Forsyth, D., & Uyeda, S. (1975). On the relative importance of the driving forces of plate motion. *Geophysical Journal International*, *43*(1), 163–200. https://doi.org/10.1111/j.1365-246X.1975.tb00631.x

Forsyth, D. W., & Li, A. (2005). Array analysis of two-dimensional variations in surface wave phase velocity and azimuthal anisotropy in the presence of multipathing interference. *Geophysical Monograph-American Geophysical Union*, *157*, 81. https://doi.org/10.1029/156GM06

French, S. W., & Romanowicz, B. A. (2014). Whole-mantle radially anisotropic shear velocity structure from spectral-element waveform tomography. *Geophysical Journal International*, *199*(3), 1303–1327. https://doi.org/10.1093/gji/ggu334

Gaherty, J. B. (2004). A surface wave analysis of seismic anisotropy beneath eastern North America. *Geophysical Journal International*, *158*(3), 1053–1066. https://doi.org/10.1111/j.1365-246X.2004.02371.x

Gaherty, J. B., Jordan, T. H., & Gee, L. S. (1996). Seismic structure of the upper mantle in a Central Pacific corridor. *Journal of Geophysical Research*, *101*(B10), 22,291–22,309.

Gao, H. (2016). Seismic velocity structure of the Juan de Fuca and Gorda plates revealed by a joint inversion of ambient noise and regional earthquakes. *Geophysical Research Letters*, *43*, 5194–5201. https://doi.org/10.1002/2016GL069381

Hastings, W. K. (1970). Monte Carlo sampling methods using Markov chains and their applications. *Biometrika*, *57*(1), 97–109. http://doi.org/10.1093/biomet/57.1.97

Hawley, W. B., Allen, R. M., & Richards, M. A. (2016). Tomography reveals buoyant asthenosphere accumulating beneath the Juan de Fuca plate. *Science*, *353*(6306), 1406–1408. https://doi.org/10.1126/science.aad8104

Hedjazian, N., Garel, F., Davies, D. R., & Kaminski, E. (2017). Age-independent seismic anisotropy under oceanic plates explained by strain history in the asthenosphere. *Earth and Planetary Science Letters*, *460*, 135–142. https://doi.org/10.1016/j.epsl.2016.12.004

Hirth, G., & Kohlstedt, D. L. (1996). Water in the oceanic upper mantle: Implications for rheology, melt extraction and the evolution of the lithosphere. *Earth and Planetary Science Letters*, *144*(1–2), 93–108. https://doi.org/10.1016/0012-821X(96)00154-9

Holtzman, B. K., & Kendall, J. M. (2010). Organized melt, seismic anisotropy, and plate boundary lubrication. *Geochemistry, Geophysics, Geosystems*, *11*, Q0AB06. https://doi.org/10.1029/2010GC003296

Holtzman, B. K., Kohlstedt, D. L., Zimmerman, M. E., Heidelbach, F., Hiraga, T., & Hustoft, J. W. (2003). Melt segregation and strain partitioning: Implications for seismic anisotropy and mantle flow. *Science*, *301*(5637), 1227–1230. http://doi.org/10.1126/science.1087132

Ismaïl, W. B., & Mainprice, D. (1998). An olivine fabric database: An overview of upper mantle fabrics and seismic anisotropy. *Tectonophysics*, *296*(1–2), 145–157.

Janiszewski, H. A., Gaherty, J. B., Abers, G. A., Gao, H., & Eilon, Z. C. (2019). Amphibious surface-wave phase-velocity measurements of the Cascadia subduction zone. *Geophysical Journal International*, *217*(3), 1929–1948. https://doi.org/10.1093/gji/ggz051

Kaminski, É., & Ribe, N. M. (2002). Timescales for the evolution of seismic anisotropy in mantle flow. *Geochemistry, Geophysics, Geosystems*, *3*(8), 1051. https://doi.org/10.1029/2001GC000222

Karato, S., Jung, H., & Katayama, I. (2008). Geodynamic significance of seismic anisotropy of the upper mantle: New insights from laboratory studies. *Annual Review of Earth and Planetary Sciences*, *36*(1), 59–95. https://doi.org/10.1146/annurev.earth.36.031207.124120

Katz, R. F. (2010). Porosity-driven convection and asymmetry beneath mid-ocean ridges. *Geochemistry, Geophysics, Geosystems*, *11*, Q0AC07. https://doi.org/10.1029/2010GC003282

Katz, R. F., Spiegelman, M., & Holtzman, B. (2006). The dynamics of melt and shear localization in partially molten aggregates. *Nature Geoscience*, *442*, 676–679.

Keller, T., Katz, R. F., & Hirschmann, M. M. (2017). Volatiles beneath mid-ocean ridges: Deep melting, channelised transport, focusing, and metasomatism. *Earth and Planetary Science Letters*, *464*, 55–68. https://doi.org/10.1016/j.epsl.2017.02.006

Kendall, J. M., Stuart, G. W., Ebinger, C. J., Bastow, I. D., & Keir, D. (2005). Magma-assisted rifting in Ethiopia. *Nature Geoscience*, *433*(7022), 146–148.

Kreemer, C., Blewitt, G., & Klein, E. C. (2014). A geodetic plate motion and global strain rate model. *Geochemistry, Geophysics, Geosystems*, *15*, 3849–3889. https://doi.org/10.1002/2014GC005407

Lin, P., Gaherty, J. B., Jin, G., Collins, J. A., & Lizarralde, D. (2016). High-resolution seismic constraints on flow dynamics in the oceanic asthenosphere. *Nature Geoscience*, *535*, 438–541.

Long, M. D., & Becker, T. W. (2010). Mantle dynamics and seismic anisotropy. *Earth and Planetary Science Letters*, *297*, 341–354. https://doi.org/10.1016/j.epsl.2010.06.036

Mainprice, D., & Nicolas, A. (1989). Development of shape and lattice preferred orientations: Application to the seismic anisotropy of the lower crust. *Journal of Structural Geology*, *11*(1–2), 175–189.

Martin-Short, R., Allen, R. M., Bastow, I. D., & Totten, E. (2015). Mantle flow geometry from ridge to trench beneath the Gorda-Juan de Fuca plate system. *Nature Geoscience*, *8*(12), 965–968. https://doi.org/10.1038/ngeo2569

Metropolis, N., & Rosenbluth, A. W. (1953). Equation of state calculations by fast computing machines. *The Journal of Chemical Physics*, *21*(6), 1087–1092.

Mondal, P., & Long, M. D. (2019). A model space search approach to finite-frequency SKS splitting intensity tomography in a reduced parameter space. *Geophysical Journal International*, *217*(1), 238–256. http://doi.org/10.1093/gji/ggz016

Montagner, J. P., & Nataf, H. C. (1986). A simple method for inverting the azimuthal anisotropy of surface waves. *Journal of Geophysical Research*, *91*(B1), 511–520.

Montagner, J. P., & Tanimoto, T. (1991). Global upper mantle tomography of seismic velocities and anisotropies. *Journal of Geophysical Research*, *96*(B12), 20,337–20,351. https://doi.org/10.1029/91JB01890/pdf

Mosher, S. G., Audet, P., & L'Heureux, I. (2014). Seismic evidence for rotating mantle flow around subducting slab edge associated with oceanic microplate capture. *Geophysical Research Letters*, *41*, 4548–4553. http://doi.org/10.1002/2014GL060630

Moulik, P., & Ekström, G. (2014). An anisotropic shear velocity model of the Earth's mantle using normal modes, body waves, surface waves and long-period waveforms. *Geophysical Journal International*, *199*(3), 1713–1738. https://doi.org/10.1093/gji/ggu356

Moulik, P., Lekić, V., Ekström, G., & Romanowicz, B. (2019). Earth's bulk structure and heterogeneity from big data and full-spectrum tomography, AGU Fall Meeting 2019, Abstract #U42B–03

Nettles, M., & Dziewonski, A. M. (2008). Radially anisotropic shear velocity structure of the upper mantle globally and beneath North America. *Journal of Geophysical Research*, *113*, B02303. https://doi.org/10.1029/2006JB004819

Nicolas, A., & Christensen, N. I. (1987). Formation of anisotropy in upper mantle peridotites: A review. *Geodynamics Series*, *16*, 111–123.

Nishimura, C. E., & Forsyth, D. W. (1989). The anisotropic structure of the upper mantle in the Pacific. *Geophysical Journal International*, *96*(2), 203–229. https://doi.org/10.1111/j.1365-246X.1989.tb04446.x

Nowacki, A., Kendall, J. M., & Wookey, J. (2012). Mantle anisotropy beneath the Earth's mid-ocean ridges. *Earth and Planetary Science Letters*, *317*, 56–67.

Rau, C. J., & Forsyth, D. W. (2011). Melt in the mantle beneath the amagmatic zone, *southern Nevada. Geology*, *39*(10), 975–978. http://doi.org/10.1130/G32179.1

Ruan, Y., Forsyth, D. W., & Bell, S. W. (2018). Shear attenuation beneath the Juan de Fuca plate: Implications for mantle flow and dehydration. *Earth and Planetary Science Letters*, *496*, 189–197. https://doi.org/10.1016/j.epsl.2018.05.035

Russell, J. B., Gaherty, J. B., Lin, P.-Y. P., Lizarralde, D., Collins, J. A., Hirth, G., & Evans, R. L. (2019). High-resolution constraints on Pacific upper mantle petrofabric inferred from surface-wave anisotropy. *Journal of Geophysical Research: Solid Earth*, *35*, 415–427. https://doi.org/10.1029/2018JB016598

Rychert, C. A., Harmon N., & Tharimena S. (2018). Scattered wave imaging of the oceanic plate in Cascadia. *Science Advances*, *4*(2), eaao1908. https://doi.org/10.1126/sciadv.aao1908

Schaeffer, A. J., Lebedev, S., & Becker, T. W. (2016). Azimuthal seismic anisotropy in the Earth's upper mantle and the thickness of tectonic plates. *Geophysical Journal International*, *207*(2), 901–933. https://doi.org/10.1093/gji/ggw309

Silver, P. G., & Chan, W. W. (1991). Shear wave splitting and subcontinental mantle deformation. *Journal of Geophysical Research*, *96*(B10), 16,429–16,454.

Skemer, P., & Hansen, L. N. (2016). Inferring upper-mantle flow from seismic anisotropy: An experimental perspective. *Tectonophysics*, *668-669*(C), 1–14. https://doi.org/10.1016/j.tecto.2015.12.003

Smith, M. L., & Dahlen, F. A. (1973). The azimuthal dependence of Love and Rayleigh wave propagation in a slightly anisotropic medium. *Journal of Geophysical Research*, *78*(17), 3321–3333.

Takeo, A., Kawakatsu, H., Isse, T., & Nishida, K. (2016). Seismic azimuthal anisotropy in the oceanic lithosphere and asthenosphere from broadband surface wave analysis of OBS array records at 60 Ma seafloor. *Journal of Geophysical Research: Solid Earth*, *121*, 1927–1947. https://doi.org/10.1002/2015JB012429/pdf

Takeo, A., Kawakatsu, H., Isse, T., Nishida, K., Shiobara, H., Sugioka, H., et al. (2018). In-situ characterization of the lithosphere-asthenosphere system beneath NW Pacific Ocean via broadband dispersion survey with two OBS arrays. *Science*, 1–24. http://doi.org/10.1029/2018GC007588

Toomey, D., Allen, R., Barclay, A., Bell, S., Bromirski, P., Carlson, R., et al. (2014). The Cascadia Initiative: A sea change in seismological studies of subduction zones. *Oceanography*, *27*(2), 138–150. https://doi.org/10.5670/oceanog.2014.49

Toomey, D. R., Jousselin, D., Dunn, R. A., Wilcock, W. S. D., & Detrick, R. S. (2007). Skew of mantle upwelling beneath the East Pacific Rise governs segmentation. *Nature*, *446*(7134), 409–414. http://doi.org/10.1038/nature05679

Turner, A. J., Katz, R. F., & Behn, M. D. (2015). Grain-size dynamics beneath mid-ocean ridges: Implications for permeability and melt extraction. *Geochemistry, Geophysics, Geosystems*, *16*, 925–946. https://doi.org/10.1002/2014GC005692

VanderBeek, B. P., & Toomey, D. R. (2017). Shallow mantle anisotropy beneath the Juan de Fuca plate. *Geophysical Research Letters*, *44*, 11,382–11,389. https://doi.org/10.1002/2017GL074769

VanderBeek, B. P., Forsyth, D. W., & Toomey, D. R. (2019). New Constraints on Mantle Shear Velocity Structure Offshore Cascadia from the Joint Analysis of Teleseismic Body and Rayleigh Wave Data [abstract]. In: Seismological Society of America Annual Meeting; 2019 April 23-26; Seattle, WA. Seismological Research Letters 90(2B), 916.

VanderBeek, B. P., & Toomey, D. R. (2019). *Pn* Tomography of the Juan de Fuca and Gorda Plates: Implications for mantle deformation and hydration in the oceanic lithosphere. *Journal of Geophysical Research: Solid Earth*, *124*, 8565–8583. https://doi.org/10.1029/2019JB017707

VanderBeek, B. P., Toomey, D. R., Hooft, E. E. E., & Wilcock, W. S. D. (2016). Segmentation of mid-ocean ridges attributed to oblique mantle divergence. *Nature Geoscience*, *9*(8), 636–642. https://doi.org/10.1038/ngeo2745

Wang, S., Yu, H., Zhang, Q., & Zhao, Y. (2018). Absolute plate motions relative to deep mantle plumes. *Earth and Planetary Science Letters*, *490*, 88–99. http://doi.org/10.1016/j.epsl.2018.03.021

Weeraratne, D. S., Forsyth, D. W., Yang, Y., & Webb, S. C. (2007). Rayleigh wave tomography beneath intraplate volcanic ridges in the South Pacific. *Journal of Geophysical Research*, *112*, B06303. https://doi.org/10.1029/2006JB004403

Wilson, D. S. (1989). Deformation of the so-called Gorda plate. *Journal of Geophysical Research*, *94*(B3), 3065–3075.

Wilson, D. S. (1993). Confidence intervals for motion and deformation of the Juan de Fuca plate. *Journal of Geophysical Research*, *98*(B9), 16,053–16,071. https://doi.org/10.1029/93JB01227/pdf

Wolfe, C. J., & Solomon, S. C. (1998). Shear-wave splitting and implications for mantle flow beneath the MELT region of the East Pacific Rise. *Science*, *280*(5367), 1230–1232. https://doi.org/10.1126/science.280.5367.1230

Yang, Y., & Forsyth, D. W. (2006). Regional tomographic inversion of the amplitude and phase of Rayleigh waves with 2-D sensitivity kernels. *Geophysical Journal International*, *166*(3), 1148–1160. http://doi.org/10.1111/j.1365-246X.2006.02972.x

Zandt, G., & Humphreys, E. (2008). Toroidal mantle flow through the western U.S. slab window. *Geology*, *36*(4), 295. http://doi.org/10.1130/G24611A.1

Zhou, Q., Hu, J., Liu, L., Chaparro, T., Stegman, D. R., & Faccenda, M. (2018). Western U.S. seismic anisotropy revealing complex mantle dynamics. *Earth and Planetary Science Letters*, *500*, 156–167. https://doi.org/10.1016/j.epsl.2018.08.015